DOI 10.5162/ettc2026/B5.4

Fiber-Optic Low Air Speed Sensor

Marvin Henkel[1], Christopher T. Ries[1], Frederik Braband[2], Tobias Ries[2], Simone Weber[2], Thomas Kissinger[1]

1: Institut für Prozessmess- und Sensortechnik, Technische Universität Ilmenau, PF 100565, 98693, Ilmenau, Germany
2: Airbus Helicopters Deutschland GmbH, Industriestrasse 4, 86609 Donauwörth, Germany

Abstract: A novel low air speed sensor for civil helicopters based on fiber segment interferometry (FSI) is introduced. Deflection due to air flow is converted to differential strain and thus interferometric phase signals. The sensor features a compact and robust design and is capable of measuring air speeds as low as $1\,\mathrm{m\,s^{-1}}$. The effectiveness of temperature compensation by differential signal processing was found to be about two orders of magnitude for axial and homogeneous temperature changes. The sensor sensitivity was characterized by static weight tests, yielding $4.774\,\mathrm{nm\,mg^{-1}}$ with linear behavior up to $14.14\,\mathrm{g}$. Wind tunnel tests conducted at air speeds ranging from $1\,\mathrm{m\,s^{-1}}$ to $9.7\,\mathrm{m\,s^{-1}}$ confirmed the expected quadratic dependence of deflection on air speed due to the increasing aerodynamic load.

Keywords: FSI, RRI, Low Air Speed, Interferometry

1. Introduction

A longstanding limitation in rotorcraft operation is the reduced reliability of Pitot systems at low air speeds in providing accurate measurements of air speed and wind direction. This involves significant challenges for pilots during hovering operations, where yaw stability is compromised, and in severe cases may lead to a vortex ring state. Therefore, low air speed instrumentation helps pilots avoid unfavorable aerodynamic conditions. However, standard Pitot systems are not suitable because of insufficient dynamic pressure and downwash induced errors below approximately 30 kn [8]. To address this problem, various solutions, each with their own disadvantages, have been presented. For example, rotating differential pressure sensors mounted on the rotor itself are complex and expensive, while hot-wire anemometers can fail due to dust or insects [2, 8]. This need led to the development of the low air speed sensor presented here, based on patent application EP25159432.1 from Airbus Helicopters. The sensor takes advantage of a relatively low cost and low complexity fiber segment interferometry (FSI) system [7] and a simple, robust cantilever design, promising immunity to electromagnetic fields (i.e. lightning), resistance to dust and insects and highly sensitive interferometric data acquisition. Also, FSI was previously used on harsh helicopter environments [4]. The principle of FSI is based on range-resolved interferometry (RRI), introduced in 2015, which employs sinusoidal wavelength modulation of highly coherent and cost-effective laser diodes from the telecommunications industry to simultaneously demodulate multiple interferometers with different optical path lengths [5]. FSI is an RRI application for fiber segments defined between backreflections within the optical fiber, either induced by inscribed fiber Bragg gratings or by Fresnel reflections at flat-cleaved fiber ends. Strain-induced changes of segment length lead to phase changes in the interferometric signal. In a configuration of four fibers in a 90° arrangement on a round cantilever, the differential phase signal of the opposite fibers can be used for highly dynamic shape sensing [6]. The presented sensor features a simple one-segment FSI design focusing on tip deflection of a round cantilever induced by air movement relative to the sensor.

2. Theory and Sensor Design

As shown in Figure 1(a), the basic principle of the sensor is a simple round cantilever, which is exposed to ambient airflow. The air flow induces a distributed load to the sensor depending on its shape and projected surface, which are considered constant, and the air speed of the approaching airflow. Thus, one can measure the bending of the cantilever and trace it back to the air speed. As shown in Figure 1(b), the sensor consists of an inner round aluminum bar with standard SMF-28 optical fiber longitudinally superglued onto it in a 90 degree arrangement, which is then inserted into an outer aluminum tube.

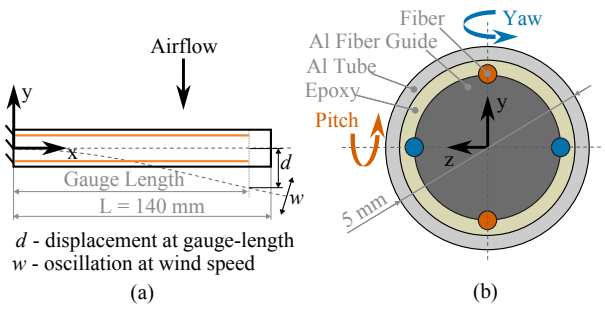


Figure 1: Sensor Design: **(a)** Schematic of cantilever beam, **(b)** cross sectional view shows 4-fiber arrangement.

The emerging cavity between the bar and the tube is filled with epoxy. The materials and dimensions define the sensors stiffness and strain transmission to the fibers and thus its

DOI 10.5162/ettc2026/B5.4

sensitivity. For each fiber, the interrogated FSI segment is formed by the back-reflections generated at the cleaved fiber tip and at the non-angled pigtail connector fixed within the sensor mount. As the clamping is considered perfectly rigid, the effective gauge length equals the distance from the clamping to the fiber ends. To guarantee a Fresnel reflection at the fiber ends even in harsh environments, the support structure is slightly extended beyond the fibers. The sensors end is then sealed watertight by gluing in a plug, ensuring a glass-air transition.

Using the Euler-Bernoulli beam theorem, one can simplify the bending of the sensor to a planar mechanical problem. As the cross section of the beam is considered constant, the distributed load on the projected area q_0 can be further simplified to the line load q:

$$q = \frac{q_0}{\mathrm{L}} = \frac{1}{2}\rho v^2 \mathrm{c_w} \mathrm{D_{Sensor}} \tag{1}$$

where D_{Sensor} is the sensors diameter, ρ is the density of the streaming air, $\mathrm{c_w}$ is the drag coefficient of the sensor, v is the air speed and L is the length of the sensor. Assuming Reynolds numbers in a range of $300 \leq Re \leq 3300$ for low air speeds between $1\,\mathrm{m\,s^{-1}}$ and $10\,\mathrm{m\,s^{-1}}$, the drag coefficient is selected at $\mathrm{c_w} = 1.0$ and considered constant based on data from [1]. By dividing v in its y-direction part v_{pitch} and its z-direction part v_{yaw} and thus dividing q in q_{pitch} and q_{yaw}, the displacement of the sensors tip in either axis $d_{\mathrm{tip_{pitch}}}$ and $d_{\mathrm{tip_{yaw}}}$ can be written as follows:

$$d_{\mathrm{tip}_i} = \frac{q_i}{\mathrm{S_b}} \mathrm{L}^4 \tag{2}$$

Where $\mathrm{S_b}$ is the effective bending stiffness, derived from:

$$\mathrm{S_b} = \mathrm{E_{Al,inner}} \mathrm{I_{Al,inner}} + \mathrm{E_{Epoxy}} \mathrm{I_{Epoxy}} + \mathrm{E_{Al,outer}} \mathrm{I_{Al,outer}} \tag{3}$$

E_i is the Young's modulus and I_i is the moment of inertia for each layer of the sensor, respectively. The influence of the 125 µm fiber is considered negligible. The deflection at gauge length d_{gauge} can be calculated as follows:

$$d_{\mathrm{gauge}_i} = \frac{q_i}{24\mathrm{S_b}} \underbrace{\left(6\mathrm{L}^2\mathrm{L}_{\mathrm{gauge}}^2 - 4\mathrm{L}\mathrm{L}_{\mathrm{gauge}}^3 + \mathrm{L}_{\mathrm{gauge}}^4\right)}_{=\mathrm{K}} \tag{4}$$

By introducing factor K as shown above and substituting Equation 1 into Equation 4, the following quadratic air speed dependence can be derived:

$$d_{\mathrm{gauge}_i} = \frac{\rho \mathrm{c_w} \cdot \mathrm{D_{Sensor}} \cdot \mathrm{K}}{48\mathrm{S_b}} v_i^2 \tag{5}$$

Introducing the differential phase signal of opposite fibers $\Delta\Phi_{\mathrm{pitch}}$ and $\Delta\Phi_{\mathrm{yaw}}$ measured by FSI and correlating it to the tip displacement of simple cantilever configurations as in [3] leads to:

$$d_{\mathrm{gauge}_i} = \frac{\mathrm{L_{gauge}}\lambda_0}{6\pi \mathrm{n_g k} \cdot \delta} \Delta\Phi_{\mathrm{axis}_i} \tag{6}$$

Where λ_0 is the center wavelength of the modulated laser diode, $\mathrm{n_g}$ is the group refractive index of the fiber, k is the fiber optic strain coefficient and δ is the core pitch. Equation 6 is derived for the application of a single force at the end of a cantilever instead of a distributed load, leading to small inaccuracies, which are deemed acceptable. By equating Equation 5 and Equation 6 the air speed dependent differential phase signal can be derived for each direction as the effective sensor output, respectively:

$$\Delta\Phi_{\mathrm{axis}_i} = \underbrace{\frac{\rho \mathrm{c_w} \cdot \mathrm{D_{Sensor}} \cdot \mathrm{K}}{48\mathrm{S_b}}}_{\text{Mechanics}} \cdot \underbrace{\frac{6\pi \mathrm{n_g k} \cdot \delta}{\mathrm{L_{gauge}}\lambda_0}}_{\text{Interferometry}} \cdot \underbrace{v_i^2}_{\text{Target}} \tag{7}$$

However, for ease of discussion, the calculated displacement at gauge length will be considered in the following.

The assumed nominal fiber parameters are $\mathrm{n_g} = 1.47$ and $\mathrm{k} = 0.7951$ [9]. The diameter and length of the sensor were selected in a way that a relatively compact but also robust sensor is achieved and standard dimensions for rods and tubes can be used. Furthermore, the sensor must be capable of measuring air speeds as low as $2.5\,\mathrm{kn} = 1.29\,\mathrm{m\,s^{-1}}$ and withstand air speeds of $220\,\mathrm{kn} = 113.18\,\mathrm{m\,s^{-1}}$. The available space on common civil helicopters limits the sensor length to a maximum of 140 mm. For manufacturing purposes and to leave space for closing up the sensor end, the gauge length is specified 22 mm shorter than the sensor length. Due to availability from scale model building, an outer tube of dimensions $5\,\mathrm{mm} \times 0.425\,\mathrm{mm}$ is used for the prototype presented. It is made of a standard aluminum alloy with a Young's modulus of around 68 GPa. For the inner rod, a diameter of 3.5 mm turned out to be relatively practical during the manual manufacturing process and tight enough to prevent an overly off-centered assembly. It is made of the same aluminum as the tube. For the final product, a high-strength aluminum alloy such as AW-7075 at a slightly higher Young's modulus of 72 GPa is necessary to withstand higher air speeds, making the sensor stiffer and thus less sensitive. To account for that, the sensor design is carried out considering high-strength aluminum, while the processing of measured data is done considering the used aluminum from scale model building. With engraved grooves on the inner rod to guide the fibers, the distance of the opposite fibers is assumed to be $\delta = 3.65\,\mathrm{mm}$.

In Figure 2 the deflection at minimal air speed and the interferometers deflection resolution for possible gauge lengths were simulated in Matlab. The ratio between minimal gauge displacement and resolution limit at a specific gauge length is the safety factor of the sensor. At a gauge length of 104 mm, the safety factor of 1.17 is considered too small due to the manual manufacturing and unknown properties of the epoxy. As the minimal displacement increases significantly steeper with gauge length than the interferometer resolution, the maximum available gauge length and thus the sensor length are chosen at 118 mm and 140 mm, respectively.

DOI 10.5162/ettc2026/B5.4

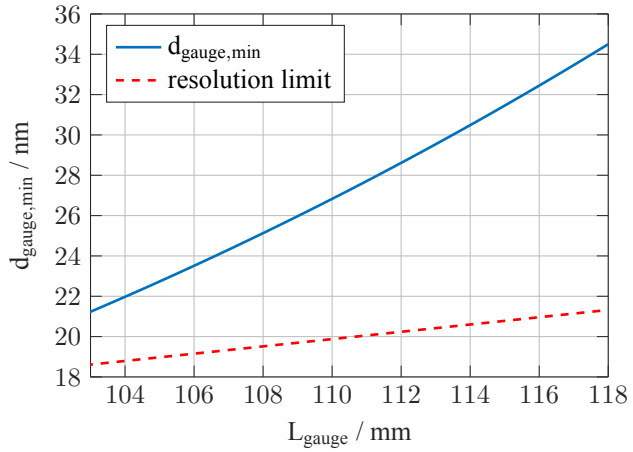


Figure 2: Minimal deflection at gauge length d_{gauge} and resolution limit considered in the sensor design process.

3. Temperature Dependence

In theory, the introduced sensor is insensitive to purely axial temperature gradients and homogeneous temperature steps, as the thermal expansion of all components occurs symmetrically and all four fibers undergo the exact same strain. However, slight imperfections due to the manufacturing process may cause errors. To investigate the sensors sensitivity to axial temperature gradients, the experimental setup shown in Figure 3(a) was used.

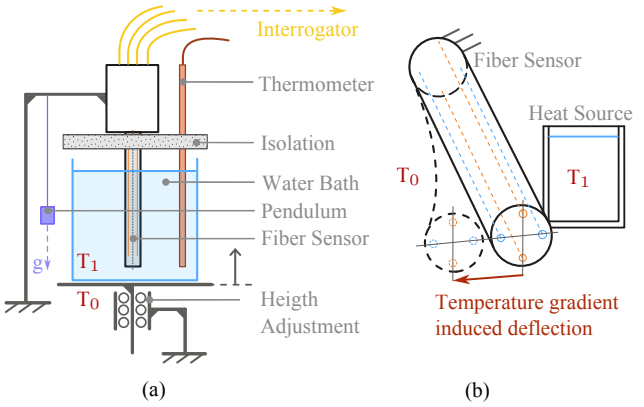


Figure 3: Temperature Supression: **(a)** no cross-sectional temperature gradient **(b)** induced cross-sectional temperature gradient due to asymmetric heating.

The clamped sensor was aligned vertically at a room temperature of 22.5 °C. In order to achieve multiple reproducible measurements, the sensor itself was fixed in place during all measurements and a heat-insulated container with water at 30 °C was lifted to the sensor by a gas spring-driven mechanism. By doing so, the sensor is gradually inserted into the water, finally reaching an end position, roughly 80% of the sensor length submerged. During this process, the sensor only undergoes axial temperature gradients that do not influence the differential phase signal of opposite fibers. However, the phase signal of a single fiber can be processed to quantify the strain induced by thermal expansion for the performed temperature step. The procedure can be reversed to produce a step from 30 °C to room temperature. The temperature is constantly measured by a PT100 resistance thermometer mounted near the sensor. The insulated container holds roughly 10 L of water. Due to the relatively high volume, the water temperature can be considered constant during all measurements. Deviations between the gravitational direction and the sensor alignment lead to buoyancy-induced axial and radial forces on the sensor. Whilst axial components theoretically cancel out due to differential phase processing, radial components result in measurable deflections. To minimize such buoyancy errors, the sensor orientation was adjusted to match the direction of gravity using a hanging pendulum. As seen in Figure 4, the processed differential phase signal step is approximately 3 rad (6.8 µm deflection) in pitch and 4 rad (9.1 µm deflection) in yaw, corresponding to a suppression of nearly two orders of magnitude. However, it does not stay zero as discussed theoretically.

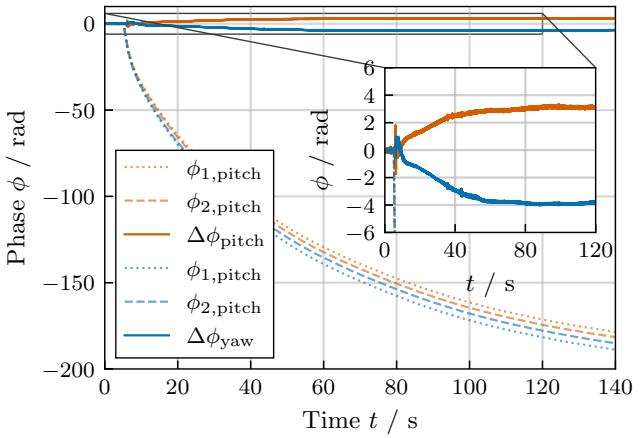


Figure 4: Step response of the individual phase signal ϕ and the differential phase signal $\Delta\phi$ for a temperature difference of 7.5 K reveals temperature suppression of ≈2 orders of magnitude.

The optical fiber is cleaved and glued by hand. Thus, a maximum gauge length deviation between the opposite fibers of 2 mm is considered. The thermal expansion of aluminum is transferred to the optical fibers. The thermal expansion ΔL is expected to be linear and can be calculated as follows:

$$\Delta L = \alpha \cdot \mathrm{L}_0 \cdot \Delta T \tag{8}$$

Where ΔT is the temperature difference between two fibers or before and after temperature changes. For 2 mm deviation between opposite fibers, assuming the thermal expansion coefficient of aluminum at $\alpha_{Al} = 24 \times 10^{-6}\ \mathrm{K}^{-1}$ and the unknown behavior of the glue to be negligible, a temperature step of 7.5 °C results in a differential thermal expansion of 360 nm, which corresponds to the deflection of 7.9 µm at gauge length, approximately reaching the measured step

DOI 10.5162/ettc2026/B5.4

in yaw and even exceeding the measured step in pitch. It is assumed that the remaining error can be greatly reduced by using better mechanical assembly fixtures and more precise cleaving methods.

In contrast to theoretically canceled out thermal expansion in axial temperature gradients and homogeneous temperature steps, radial temperature gradients, as shown in Figure 3(b), effectively lead to large errors even in theory. Assuming a fiber length of 118 mm at room temperature and a temperature difference of 2 K between the opposite fibers, the transferred thermal expansion of the aluminum leads to a great difference of 5.664 µm, corresponding to a deflection of 123.77 µm at gauge length. Thus, radial temperature gradients appear much more critical for the introduced sensor. However, as experimental setups to achieve reproducible and measurable radial temperature gradients in the sensor are way more complex than the presented setup for axial temperature gradients, this remains to be investigated.

4. Static Weight Tests

Before preparing wind tunnel experiments, the sensors capabilities were investigated in static tests. The sensor is horizontally oriented, and different magnetic weights were manufactured and attached to the sensors end, respectively. After each weight was attached, the sensor was allowed to settle for approximately 8 s to ensure the decay of oscillations. Then the measurement is started in the deflected state. The weight is then carefully removed during measurement using a strong magnet to generate as little oscillation as possible. After around 8 s, the inevitable oscillation has settled and the differential phase signals can be evaluated. For this test, the sensor was oriented such that the plane defined by the pitch fibers was aligned with the gravitational direction. Thus, evaluating only pitch signals was sufficient. The deflections mean value and standard deviation for each weight are shown in Figure 5. Weights are 9.1 mg, 15.1 mg, 21 mg, 29.7 mg, 5525.7 mg, 9733.9 mg and 14 136.5 mg and five measurements were performed for each weight, respectively.

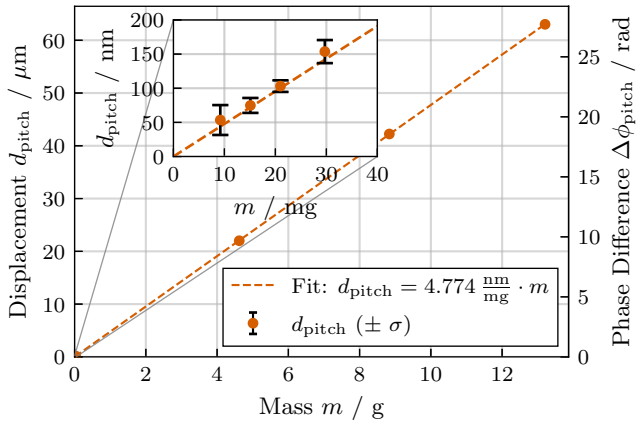


Figure 5: Sensitivity analysis: displacement d_{pitch} resulting from static weight testing over a mass range of 9.1 mg to 14 136.5 mg.

As the focus of this study is low air speed, smaller weights were considered more significant and thus, four weights resulting in differential phase signals near the sensors resolution limit were manufactured and tested. The mass m_{min} of 9.1 mg produces a gravitational force equivalent to the minimum line load q at the target minimum wind speed. A linear fit through the mean values of each weight and the origin was performed to obtain the sensors sensitivity to perpendicular forces at the sensors end. Note that for each weight, the confidence interval overlaps the linear fit. Thus, the calculated sensitivity of $4.774\,\text{nm}\,\text{mg}^{-1}$ is considered reliable. The wide range of masses demonstrates the high linearity and range of the sensor.

5. Wind Tunnel Experiments

After evaluating temperature suppression and static weight tests, wind tunnel tests were performed. Therefore, the sensor was fixed vertically and the pitch direction of the 4-fiber arrangement was aligned with the airflow according to Figure 1(a). In order to compensate for the time-consuming settling behavior of the wind tunnel, the measurement was started when a constant and homogeneous wind speed was reached. The wind tunnel was shut down after 30 s of measurement to acquire the step-response in deflection, where d_{pitch} and d_{yaw} represent the individual differential measurements. Figure 6 shows an example measurement for a velocity of $4\,\text{m}\,\text{s}^{-1}$.

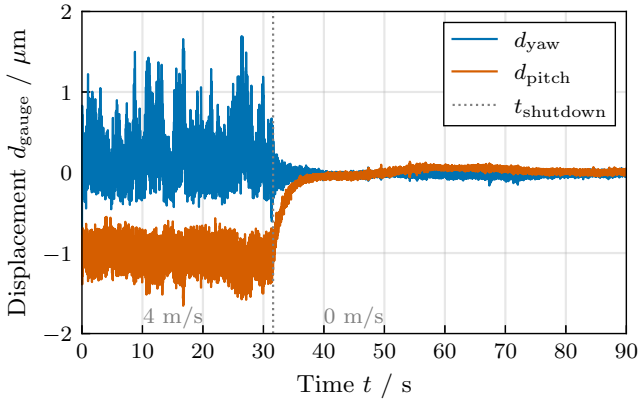


Figure 6: Directional displacement $d_{\text{pitch, yaw}}$ (low-pass filtered at a bandwidth of 120 Hz) caused by a change in wind speed from $4\,\text{m}\,\text{s}^{-1}$ to $0\,\text{m}\,\text{s}^{-1}$; the gray dotted line marks the shutdown of the wind tunnel, and the clearly visible step in d_{pitch} confirms the selected alignment of the sensor in the wind tunnel.

The differential signal of the fiber pair in pitch direction contains the air speed dependent displacement signal, while the mean signal in yaw direction remains zero. This coincides with the sensor alignment and demonstrates the capability to measure wind direction. Note that the noise in signal in the initial 30 s corresponds to real mechanical oscillations of the sensor rod, as the inherent sensor noise can be seen after the wind tunnel was shut down as is much lower. In the explained method above, a measurement series from $1\,\text{m}\,\text{s}^{-1}$ to

$9.7\,\mathrm{m\,s^{-1}}$ was performed, which can be seen in Figure 7. The measured displacements d_{gauge} in pitch and yaw direction at a given wind speed were low-pass filtered at a bandwidth of 120 Hz, followed by a moving average with a window length of 1 s. The cutoff frequency of 120 Hz was chosen, as the sensors natural frequency was calculated analytically to be 170 Hz and verified by FFT analysis to be 167 Hz. The resultant displacement is calculated as $d_{\mathrm{res}} = (d_{\mathrm{pitch}}^2 + d_{\mathrm{yaw}}^2)^{1/2}$. The quadratic fit function of d_{res} increases quadratically with rising air speed, in good agreement with the theoretical prediction (see Equation 5). The error bars visualize the oscillations $w_{\mathrm{pitch,yaw}}$ of the rod in the deflected state, which are visible in Figure 6 for a wind speed of $4\,\mathrm{m\,s^{-1}}$. Note that for higher air speeds the oscillations w_{yaw} exceed w_{pitch}.

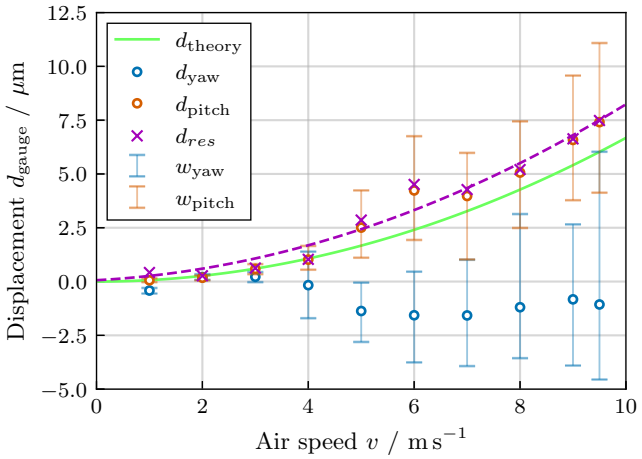


Figure 7: Measurement series reveals a quadratic dependence of the resultant displacement d_{res} to air speed v in direction of air flow in good agreement with theoretical prediction d_{theory} according to equation 5, while oscillations w_{yaw} perpendicular to airflow exceed w_{pitch} for higher air speeds.

6. Conclusion

A novel two-dimensional fiber optic low air speed sensor design based on FSI was introduced and a prototype was manufactured and tested in a small wind tunnel at air speeds ranging from $1\,\mathrm{m\,s^{-1}}$ to $9.7\,\mathrm{m\,s^{-1}}$. Errors originating from axial temperature gradients were experimentally determined and errors due to radial temperature gradients were discussed. The manufactured prototype features an aluminum rod of 3.5 mm diameter and an aluminum tube of dimensions $5\,\mathrm{mm}\times 0.425\,\mathrm{mm}$. The sensor itself is 140 mm long with a gauge length of 118 mm. It was shown that the sensitivity to homogeneous and axial temperature changes is greatly reduced by applying differential phase signal processing and that the remaining errors due to manufacturing tolerances can be reduced. The highly linear sensitivity to static forces was experimentally verified. Furthermore, in wind tunnel tests, air speeds of $1\,\mathrm{m\,s^{-1}}$ up to $10\,\mathrm{m\,s^{-1}}$ provided the expected quadratic air speed dependence of the measured displacement and the measured first order natural frequency was verified to be with good agreement to theory. For use on helicopters, future tests regarding acceleration and inertia as well as forced vibration, especially by common frequencies on helicopters, might provide crucial information.

Acknowledgement

The authors gratefully acknowledge the support by the Deutsche Forschungsgesellschaft (DFG), Germany, in the scope of the project ‘Interferometric Six Degree-of-Freedom Direct Fibre Optic Shape Sensing’ (Project Number: 536023270) at Technische Universität Ilmenau, Germany.

References

[1] H. A. Elghannay and Y. M. F. E. Hasadi. ‘Development of Drag Coefficient Correlations for Circular Cylinder Using Turingbot Symbolic Regression Software$_2$026’, *Al-Mukhtar Journal of Engineering Research* 7.1 (Apr. 2026), pp. 20–28. DOI: 10.54172/wadd2q70.

[2] D. Fujiwara and T. Tonoike. ‘Development and flight-test verification of two-dimensional rotational low-airspeed sensor for small helicopters’, *ROBOMECH Journal* 11.1 (9th Apr. 2024), p. 6. DOI: 10.1186/s40648-024-00274-2.

[3] C. Hemeling, V. Cherkasova, T. Fröhlich and T. Kissinger. ‘Self-sensing multicore fiber probe for interferometric measurement of lateral displacement and force’, *Measurement* 257 (2026), p. 118814. DOI: https://doi.org/10.1016/j.measurement.2025.118814.

[4] S. W. James, T. Kissinger, S. Weber, K. Mullaney, E. Chehura, H. H. Pekmezci, J. H. Barrington, S. E Staines, T. O. H. Charrett, N. J. Lawson, M. Lone, R. Atack and R. P. Tatam. ‘Fibre-optic measurement of strain and shape on a helicopter rotor blade during a ground run: 1. Measurement of strain’, *Smart Materials and Structures* 31.7 (1st July 2022), p. 075014. DOI: 10.1088/1361-665X/ac736d.

[5] T. Kissinger, T. O. Charrett and R. P. Tatam. ‘Range-resolved interferometric signal processing using sinusoidal optical frequency modulation’, *Opt. Express* 23.7 (Apr. 2015), pp. 9415–9431. DOI: 10.1364/OE.23.009415.

[6] T. Kissinger, E. Chehura, S. E. Staines, S. W. James and R. P. Tatam. ‘Dynamic Fiber-Optic Shape Sensing Using Fiber Segment Interferometry’, *Journal of Lightwave Technology* 36.4 (2018), pp. 917–925. DOI: 10.1109/JLT.2017.2750759.

[7] T. Kissinger, R. Correia, T. O. H. Charrett, S. W. James and R. P. Tatam. ‘Fiber Segment Interferometry for Dynamic Strain Measurements’, *Journal of Lightwave Technology* 34.19 (1st Oct. 2016), pp. 4620–4626. DOI: 10.1109/JLT.2016.2530940.

[8] C. G. Knight. *Low Airspeed Measuring Devices for Helicopter Usage Monitoring*. Technical Note DSTO-TN-0495. Fishermans Bend, Victoria, Australia: Defence Science and Technology Organisation (DSTO), May 2003.

[9] J. Roths and F. Jülich. ‘Determination of strain sensitivity of free fiber Bragg gratings’, Photonics Europe. Ed. by F. Berghmans, A. G. Mignani, A. Cutolo, P. P. Meyrueis and T. P. Pearsall. Strasbourg, France, 25th Apr. 2008, p. 700308. DOI: 10.1117/12.781426.